




RESEARCH ARTICLE | NOVEMBER 10 2023

Iron-based catholytes for aqueous redox-flow batteries


Atsushi Okazawa ; Takayuki Kakuchi; Kosuke Kawai ; Masashi Okubo 




APL Mater. 11, 110901 (2023)
<https://doi.org/10.1063/5.0160078>



18 April 2024 22:21:42



Biomicrofluidics
Special Topic:
Microfluidic Biosensors
Submit Today



Iron-based catholytes for aqueous redox-flow batteries

Cite as: APL Mater. 11, 110901 (2023); doi: 10.1063/5.0160078

Submitted: 30 May 2023 • Accepted: 23 October 2023 •

Published Online: 10 November 2023



View Online



Export Citation



CrossMark

Atsushi Okazawa,^{a)} Takayuki Kakuchi, Kosuke Kawai, and Masashi Okubo^{a)}

AFFILIATIONS

Department of Electrical Engineering and Bioscience, School of Advanced Science and Engineering, Waseda University, Okubo 3-4-1, Shinjuku-ku, Tokyo 169-8555, Japan

^{a)} Authors to whom correspondence should be addressed: okazawa.sinisa@gmail.com and m-okubo@waseda.jp

ABSTRACT

Redox-flow batteries (RFBs) are promising electrochemical energy storage devices to load-level intermittent power from renewable energy. In particular, aqueous RFBs using aqueous electrolytes possess several advantages over nonaqueous ones, such as low fabrication cost, non-toxicity, safety, and environmental benignity. Therefore, developing high-performance, abundant, less-expensive iron-based catholytes for aqueous RFBs is essential toward their wide deployment in a power grid. In this Perspective, we summarize the recent progress of iron-based catholytes for aqueous RFBs. We emphasize that iron-based catholytes possess widely ranged redox potentials (−1.0 to 1.5 V vs standard hydrogen electrodes) and solubility in water (0.2–4.0 mol L^{−1}), thereby providing a wide range of cell performance. The molecular design, such as ligand functionalization, counter ion mixing, and asymmetrization, allows for rationally improving solubility, redox potential, and energy density. Furthermore, we demonstrate a simple evaluation method of the redox potential of iron-based catholytes using the calculated energy levels of the lowest unoccupied molecular orbital of ligand molecules. Finally, we rationalize the design strategy of iron-based catholytes for advanced aqueous RFBs.

© 2023 Author(s). All article content, except where otherwise noted, is licensed under a Creative Commons Attribution (CC BY) license (<http://creativecommons.org/licenses/by/4.0/>). <https://doi.org/10.1063/5.0160078>

I. INTRODUCTION

For sustainable development, electricity generated from renewable energy sources, such as solar and wind, must be integrated into power grids as an alternative to fossil fuels. However, the generated power supply is intrinsically intermittent, whereby load leveling using large-scale, efficient, and low-cost energy storage technology is required. Although state-of-the-art lithium-ion batteries (LIBs) are capable of efficient energy storage using lithium-ion intercalation chemistry, their flammable electrolytes and costly cathodes impede grid-scale use of LIBs.^{1–4} In contrast, redox-flow batteries (RFBs) are promising electrochemical energy storage devices for grid-scale use because energy conversion and storage are decoupled: conversion between electric and chemical energies is conducted at electrodes in a battery cell, while chemical energy is stored in outer tanks (Fig. 1). Therefore, it is possible to flexibly design RFBs of required power and energy by adjusting the size/shape of the electrodes and tanks.

The volumetric energy density of RFB, U_{RFB} (Wh L^{−1}), is given by

$$U_{\text{RFB}} = \frac{(E_c - E_a)Q}{V_c + V_a + V_0}, \quad (1)$$

where E_c and E_a (V) are the average electrode potentials of the catholyte and anolyte and V_c , V_a , and V_0 (l) are the volumes of the catholyte tank, anolyte tank, and other cell components, respectively. Q (Ah) is the capacity of the RFB cell defined as

$$Q = n_c F C_c V_c = n_a F C_a V_a, \quad (2)$$

where n_c and n_a are the numbers of electrons in the redox reactions of the catholyte and anolyte, F (C mol^{−1}) is the Faraday constant, and C_c and C_a (mol L^{−1}) are the concentrations of the catholyte and anolyte, respectively. Straightforward strategies to increase the energy density, U_{RFB} , are to achieve (1) higher E_c , (2) lower E_a , (3) larger n_c , (4) larger n_a , (5) higher C_c , and (6) higher C_a . Extensive exploration for redox-active materials (catholytes and anolytes), electrolyte solvents, and separators for RFBs (Table I) has shown that aqueous RFBs using aqueous electrolytes exhibit

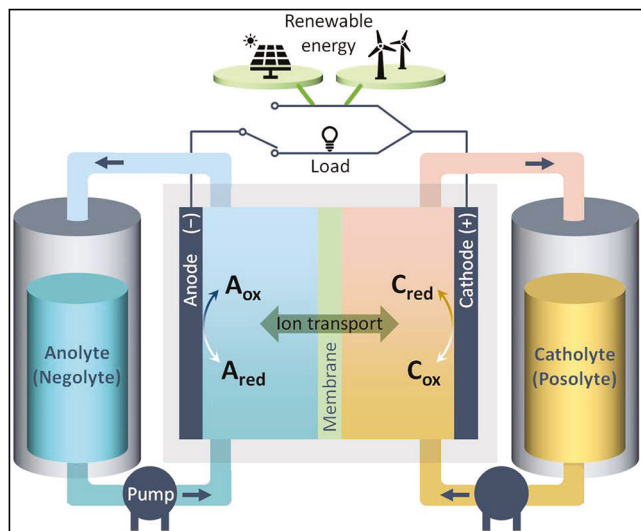


FIG. 1. Schematic representation of a redox flow battery cell. A_{ox}/A_{red} and C_{ox}/C_{red} represent oxidized/reduced species in anolyte and catholyte, respectively. Gray arrows indicate the direction of the solution flow.

multiple advantages over non-aqueous electrolytes.^{5–9} The use of water allows for the fabrication of a low-cost, nontoxic, safe (non-flammable), and environmentally benign system, conforming to several requirements for grid-scale use. For example, aqueous RFBs

consisting of a V^{3+}/V^{2+} anolyte and VO_2^+/VO^{2+} catholyte have been commercialized.

However, water possesses a narrow electrochemical potential window (~ 1.23 V), severely restricting the operating voltage of RFBs, $E_c - E_a$, to a small value and resulting in a low energy density (U_{RFB}) (Fig. 2). Thus, suppressing side reactions, such as oxygen evolution and hydrogen evolution, are necessary to achieve a high U_{RFB} with a high-voltage catholyte and/or low-voltage anolyte. Another important issue to be addressed is the development of highly soluble redox-active materials comprising abundant elements. From a cost point of view, the most preferable redox-active materials for catholytes are iron complexes. Consequently, various iron complexes have been reported for aqueous RFB catholytes [Fig. 3(a)].

In this Perspective, we summarize the recent progress in the development of the iron-based catholytes for aqueous RFBs (see Fig. 2). Based on the relationship between their electrochemical and structural/electronic properties, we rationalize the design strategy of high-performance iron-based catholytes for advanced aqueous RFBs.

II. IRON-BASED CATHOLYTES

Iron-based redox-active materials have several advantages, including elemental abundance, low cost, and low toxicity. The first all-iron RFB¹⁰ employed the following catholyte and anolyte reactions:

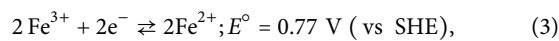


TABLE I. Summary of representative redox-flow batteries for varied systems.

Type of electrolytes	Anolyte ^a Catholyte ^a Reference	(Representative example)	
		Pros	Cons
All inorganic system	V^{3+}/V^{2+} VO_2^+/VO^{2+} Reference 5	<ul style="list-style-type: none"> • In practical use • High energy density 	<ul style="list-style-type: none"> • Sulfuric acid solution • High cost of vanadium • Crossover (self-discharge)
Metal complex system	$[Fe(TEOA)(OH)]^-$ $Na_4[Fe(CN)_6]$ Reference 6	<ul style="list-style-type: none"> • Tailorable active materials • High voltage 	<ul style="list-style-type: none"> • Low solubility in electrolytic solution
Organic/inorganic system	2,6-DHAQ $K_4[Fe(CN)_6]$ Reference 7	<ul style="list-style-type: none"> • Low cost of active materials 	<ul style="list-style-type: none"> • Strong alkaline solution • Low solubility in electrolytic solution
All organic system	TEMPOL MV Reference 8	<ul style="list-style-type: none"> • Low cost of active materials • Chemical modification 	<ul style="list-style-type: none"> • Low voltage efficiency • Low solubility in electrolytic solution
All polymer system	Viol polymer TEMPO polymer Reference 9	<ul style="list-style-type: none"> • Low cost of separator • No crossover 	<ul style="list-style-type: none"> • Low capacity

^aAbbreviations: TEOA, triethanolamine; 2,6-DHAQ, 2,6-dihydroxyanthraquinone; MV, 1,1'-dimethyl-4,4'-bipyridinium; Viol polymer, poly(*N*-4-vinylbenzyl-*N'*-methyl-4,4'-bipyridinium dichloride-co-4-vinylbenzyl); and TEMPO polymer, poly(2,2,6,6-tetramethylpiperidinyloxy-4-yl methacrylate-co-[2-(methacryloyloxy) ethyl]trimethylammonium chloride).

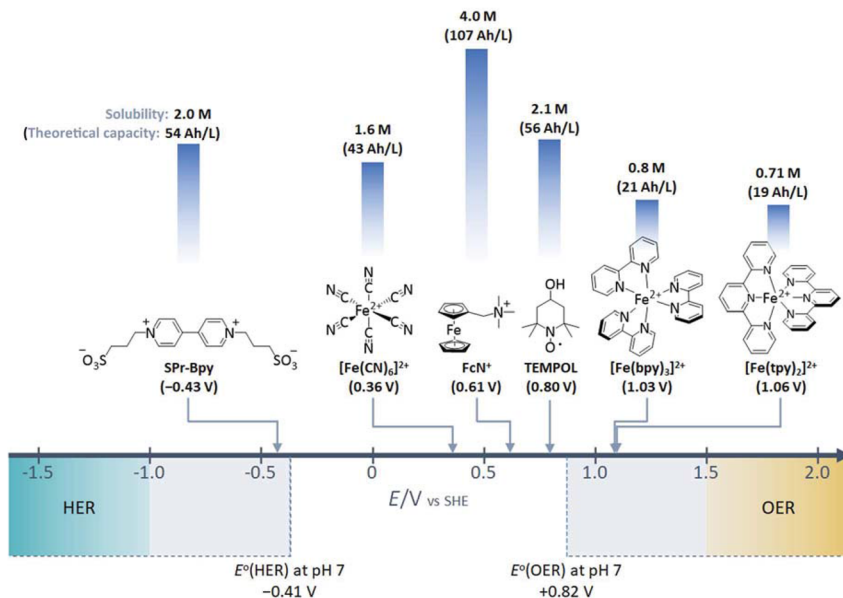


FIG. 2. Standard potential diagram (vs SHE) of representative redox-active compounds among organic molecules or iron complexes. Gray regions enclosed with broken lines show the potential ranges where hydrogen and oxygen evolution reactions (HER and OER, respectively) occur thermodynamically at pH 7. In the regions, colored realms represent the potentials expected for kinetic HER and OER using glassy carbon electrodes in a typical electrolyte, such as 0.5 M NaCl.²⁰ Blue bars indicate the solubility of the compounds. Note that the potentials and solubilities of $[\text{Fe}(\text{tpy})_2]^{2+}$ and $[\text{Fe}(\text{bpy})_3]^{2+}$ are the reported values in 0.5 M H_2SO_4 aqueous solution. SPPr-Bpy, 1,1'-bis(3-sulfonatopropyl)-4,4'-bipyridinium; FcN^+ , (Ferrocenylmethyl)trimethylammonium; TEMPOL, 4-hydroxy-2,2,6,6-tetramethylpiperidine 1-oxyl; tpy, 2,2':6',6''-terpyridine; and bpy, 2,2'-bipyridine.

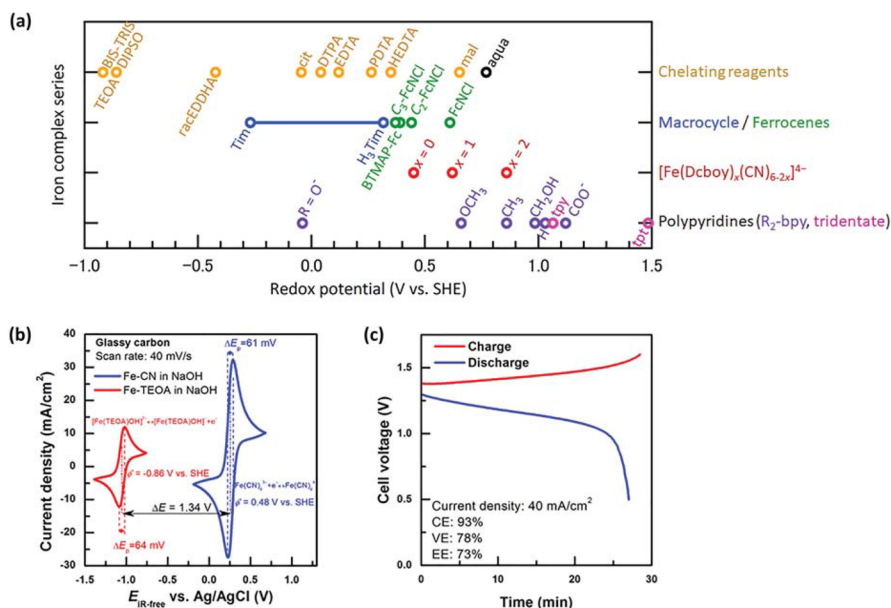
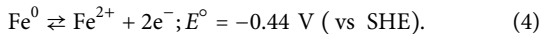


FIG. 3. (a) Formal redox potentials of the $\text{Fe}^{2+}/\text{Fe}^{3+}$ -based active materials for aqueous RFBs. The potentials are converted to SHE. The abbreviations are listed in Table II. (b) Cyclic voltammograms of $[\text{Fe}(\text{TEOA})\text{OH}]^{2+}/[\text{Fe}(\text{TEOA})\text{OH}]^{+}$ and $[\text{Fe}(\text{CN})_6]^{3-}/[\text{Fe}(\text{CN})_6]^{4-}$ in NaOH solution. (c) Charge-discharge curves of all-Fe RFB at a current density of 40 mA/cm^2 . Panels (b) and (c) are adapted with permission from Gong *et al.*, ACS Energy Lett. 1, 89–93 (2016). Copyright 2016 American Chemical Society.



Here, the anolyte reaction is iron plating/stripping, whereas the RFB system achieved an operating voltage of 1.21 V with a Coulombic efficiency of 90%. Notably, the standard electrode potentials of iron complexes are strongly influenced by their coordination ligands. Figure 3(a) summarizes various iron complexes as active materials for aqueous RFBs,^{6,11–24} where the redox potential widely ranges from -0.86 to 1.48 V vs standard hydrogen electrode (SHE).⁶ For example, using an exceptionally low-potential Fe-based anolyte $[\text{Fe}(\text{TEOA})(\text{OH})]^-$ (TEOA = triethanolamine) (-0.86 V vs SHE) resulted in a high-voltage all-iron aqueous RFB system that demonstrated an operating voltage of 1.34 V [Fig. 3(b)] with a Coulombic efficiency of 93% and low polarization below 0.3 V, maintaining a high energy efficiency of 73% even at a high current density of 40 mA cm^{-2} [Fig. 3(c)].⁶ To date, coordination compounds based on the $\text{Fe}^{2+}/\text{Fe}^{3+}$ redox couple for aqueous anolytes have been rarely found, except for $[\text{Fe}(\text{racEDDHA})]^{12,25}$ and the complexes using TEOA⁶ or its derivatives.^{11,26,27} It is due to the intrinsic high potential (0.77 V vs SHE) of the $\text{Fe}^{2+}/\text{Fe}^{3+}$ redox couple in aqueous solution.

Representative redox couples for iron-based catholytes of aqueous RFBs are shown in Fig. 4. It should be noted that a required energy density for practical application is $\sim 25\text{--}35 \text{ Wh L}^{-1}$, which is typical of commercial vanadium RFBs.^{28,29} Furthermore, the fade rate of the capacity of active materials is required to be lower than $0.1\% \text{ day}^{-1}$.³⁰ Ferrocyanides and ferrocenes are the most commonly used iron-based catholytes owing to their commercial availability and robustness against charge/discharge cycling. For example, a ferrocyanide catholyte was adopted in an alkaline quinone flow battery:⁷ the flow cell test demonstrated a capacity retention of 99% per cycle during 100 cycles at a current density of 100 mA cm^{-2} [Fig. 5(a)]. However, as ferrocene hardly dissolves in water, introducing ammonium moieties is necessary to improve its water solubility when used as a catholyte. Indeed, (ferrocenylmethyl)trimethylammonium chloride (FcNCl) exhibits a high solubility of 4.0 M in water,²⁰ and an aqueous RFB consisting of a 0.7 M FcNCl catholyte and 0.7 M methyl viologen anolyte delivers

an energy density of 9.9 Wh L^{-1} and a capacity retention of 81% after 500 cycles [Fig. 5(b)]. Furthermore, an aqueous RFB consisting of a 1.3 M 1,1'-bis(3-(trimethylammonio)propyl)ferrocene dichloride (BTMAP-Fc) catholyte and 1.3 M bis(3-trimethylammonio)propyl viologen tetrachloride (BTMAP-Vi) anolyte achieved a capacity retention of 99.9943% per cycle corresponding to a daily capacity degradation of 0.10% [Fig. 5(c)].²¹

Other major iron-coordination complexes are polypyridine- or polyimine-coordinated compounds, such as $[\text{Fe}(\text{bpy})_3]^{2+}$ and $[\text{Fe}(\text{tpy})_2]^{2+}$ (bpy: 2,2'-bipyridine, tpy: 2,2':6',2''-terpyridine). Generally, polypyridine-coordinated compounds possess high redox potentials relative to those of ferrocene derivatives.²² Importantly, a symmetry-breaking design, that is, iron-based complexes coordinated by 2,2'-bipyridine-4,4'-dicarboxylate (Dcbpy) and cyanide,²³ $\text{Na}_4[\text{Fe}(\text{Dcbpy})_2(\text{CN})_2]$, facilitates a high solubility of 1.09 M in water. A cell using a 1.02 M asymmetric $\text{Na}_4[\text{Fe}(\text{Dcbpy})_2(\text{CN})_2]$ catholyte and 1.2 M 1,1'-bis(3-sulfonatopropyl)-4,4'-bipyridinium (SPR-Bpy) anolyte exhibits a voltage of 1.2 V and an energy density of 12.5 Wh L^{-1} . The capacity degradation per cycle is 0.1% , corresponding to a daily decay of 2.3% over 250 cycles [Fig. 5(d)]. Recently, a new aqueous RFB using $[\text{Fe}(\text{Bhmbpy})_3]^{2+}$ (Bhmbpy = 4,4'-bis(hydroxymethyl)-2,2'-bipyridine) as a moderate-soluble catholyte paired with a BTMAP-Vi anolyte operates at near-neutral pH with an open circuit voltage (OCV) of 1.3 V .²⁴ The charge-discharge test shows a daily capacity fade rate of 0.16% [Fig. 5(e)] even at higher concentrations ($\sim 0.5 \text{ M}$).

III. SOLUBILITY

Equations (1) and (2) imply that enhanced solubility of redox-active materials increases the energy density of RFBs (U_{RFB}). Solubility is a fundamental physicochemical property of chemical species. However, its quantitative prediction is difficult, and only some qualitative empirical rules are known: (i) "like dissolves likes,"³¹ that is, a solution tends to dissolve solutes having a similar chemical structure, and (ii) a more asymmetrical molecule tends to be more dissolved

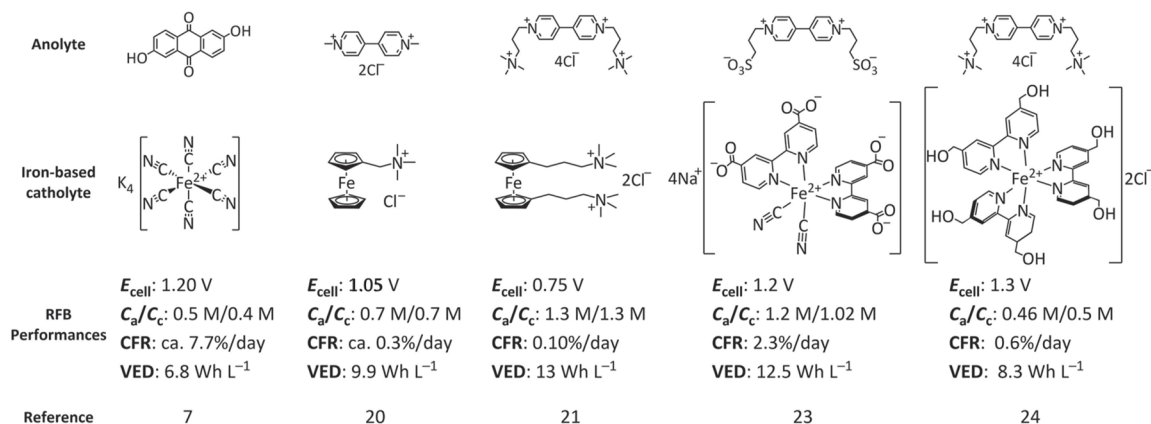


FIG. 4. Performance of aqueous RFBs using iron-based catholytes. E_{cell} : cell potential. C_a/C_c : concentrations of anolyte and catholyte, respectively. CFR: capacity fade rate in $\% \text{ day}^{-1}$. VED: Realized volumetric energy density.

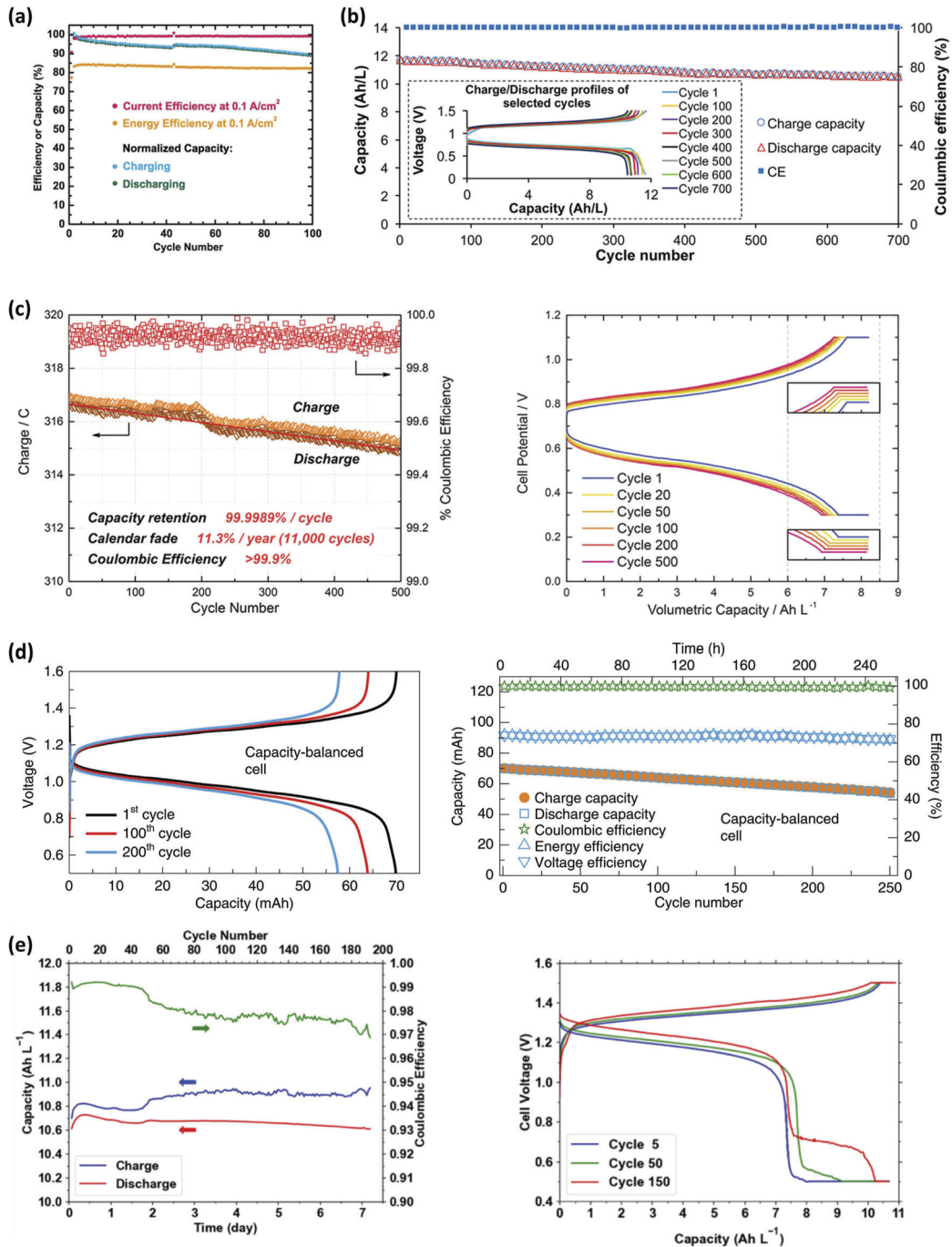


FIG. 5. Performance of aqueous RFBs using iron-based catholytes. (a) 0.4 M $K_4[Fe(CN)_6]/0.5$ M 2,6-DHAQ in 1 M KOH at 100 mA cm^{-2} . Reproduced with permission from Lin *et al.*, *Science* **349**, 1529–1532 (2015). Copyright 2015 AAAS. (b) 0.5 M $FeCl_2/MV$ in 2.0 M NaCl at 60 mA cm^{-2} . Inset: charge/discharge curves of selected cycles. Reproduced with permission from Hu *et al.*, *J. Am. Chem. Soc.* **139**, 1207–1214 (2017). Copyright 2017 American Chemical Society. (c) 0.75 M/1.00 M BTMAP-Vi/BTMAP-Fc in the presence of an excess of reduced BTMAP-Vi at 50 mA cm^{-2} . Reproduced with permission from Beh *et al.*, *ACS Energy Lett.* **2**, 639–644 (2017). Copyright 2017 American Chemical Society. (d) 1.2 M/1.02 M $Na_4[Fe(Dcbpy)_2(CN)_2]/SPPr-Bpy$ in 1.2 M NaCl and 0.4 M CH_3COONa at 24 mA cm^{-2} as a capacity-balanced RFB. Left: charge/discharge profiles. Right: charge/discharge capacity and coulombic/voltage/energy efficiencies vs cycle numbers. Reproduced with permission from Li *et al.*, *Nat. Energy* **6**, 873–881 (2021). Copyright 2018 Elsevier Inc. (e) 0.5 M/0.46 M $[Fe(Bhmbpy)_3]Cl_2/BTMAP-Vi$ in deionized water at 30 mA cm^{-2} as a catholyte capacity-limiting cell. Left: charge/discharge capacity and coulombic efficiency vs cycle numbers. Right: charge/discharge profiles. Reproduced with permission from Gao *et al.*, *Adv. Energy Mater.* **12**, 2202444 (2022). Copyright 2022 Wiley-VCH Verlag GmbH & Co. KGaA.

among similar compounds (Carnelley's rule³²).³³ Thermodynamically, the solubility (S) of a chemical species is expressed using the dissolution Gibbs energy ($\Delta_{\text{dis}}G$), which involves the sublimation Gibbs energy ($\Delta_{\text{sub}}G$) and the solvation Gibbs energy ($\Delta_{\text{sol}}G$) as

$$S = C^\circ \exp\left(-\frac{\Delta_{\text{dis}}G}{RT}\right) = C^\circ \exp\left(-\frac{\Delta_{\text{sub}}G + \Delta_{\text{sol}}G}{RT}\right), \quad (5)$$

where C° , R , and T are the molar concentration of the chemical species in the form of a solid, gas constant, and temperature, respectively.³⁴ Generally, obtaining $\Delta_{\text{sub}}G$ and C° is difficult and computationally expensive, especially for novel compounds. Thus, the solubility is commonly predicted using computed $\Delta_{\text{sol}}G$ to screen redox-active materials.^{35,36} For example, the solubility of a metal-acetylacetonate series in non-aqueous solvents was accurately predicted using non-linear regression ($R^2 = 0.79$) with features, such as the dipole moment and $\Delta_{\text{sol}}G$.³⁷

Most iron coordination complexes, especially with nonpolar aliphatic and aromatic moieties, hardly dissolve in water because their weak interaction with water and highly organized local structure of water molecules result in small $|\Delta_{\text{dis}}G|$ and, hence, small S (< 1 M). However, this drawback can be overcome by molecular designs, such as introducing hydrophilic substituents and changing counterions. (1) The substitution of ionic functional groups strongly enhances the interaction with water, leading to a highly concentrated catholyte ($S > 1$ M): the chloride salt of FeN^+ with a quaternary ammonium moiety shows an excellent water solubility of 4 M (which corresponds to a volumetric capacity of 107 Ah L^{-1}).²⁰ (2) Neutral substituents can also improve the solubility in case a large dipole moment is created in the complexes or via a hydrogen bond: $[\text{Fe}(\text{Bhmbpy})_3]^{2+}$ shows a relatively high solubility of 0.98 M in water among iron-bipyridyl complex derivatives because the hydroxymethyl groups at the 4- and 4'-position of the bpy ligands improve the solubility of the $[\text{Fe}(\text{bpy})_3]^{2+}$ complex via hydrogen bonding with water.²⁴

While potassium ferrocyanide, $\text{K}_4[\text{Fe}(\text{CN})_6]$, is widely used as a catholyte for aqueous RFBs, it has low solubility in water (~ 0.76 M). However, when the counterion is replaced with an ammonium

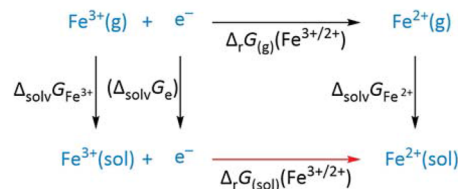


FIG. 7. Thermodynamic cycle for the calculation of the $\text{Fe}^{2+} \rightarrow \text{Fe}^{3+}$ oxidation potential in solution.

ion, the solubility drastically increases to 1.60 M (Fig. 3).³⁸ Moreover, the solubility of several ammonium salts (e.g., chloride, sulfate, carbonate, and nitrate) in water is higher than that of the corresponding sodium and potassium salts because ammonium ions can participate in the hydrogen-bond network of water. Another possibility to improve solubility is mixing Na^+ and K^+ , where the solubility of $\text{K}_4[\text{Fe}(\text{CN})_6]$ increases to 1.5 M in aqueous NaOH solution [Fig. 6(a)].³⁹ This is known as the diverse ion effect: from a microscopic point of view, additional interaction between sodium ions and ferrocyanide ions in the solution decreases $\Delta_{\text{dis}}G$ for $\text{K}_4[\text{Fe}(\text{CN})_6]$. Explicit density functional theory (DFT) calculations of solvation structures of $[\text{Fe}(\text{CN})_6]^{4-}$ demonstrated a decrease in $\Delta_{\text{sol}}G$ from 238.5 (KOH solution) to 252.9 kcal/mol (NaOH solution).

Although polypyridine-coordinated iron complexes, such as $[\text{Fe}(\text{tpy})_2]^{2+}$ and $[\text{Fe}(\text{bpy})_3]^{2+}$, generally possess low solubility in water, their PF_6^- , BF_4^- , and bis(trifluoromethanesulfonyl)imide (TFSI^-) salts can be used as redox-active materials for catholytes of non-aqueous RFBs because of their high redox potential.^{40–44} These iron complexes can also be used for the catholytes of aqueous RFBs as their chloride and sulfonate salts are soluble in water.^{22,24,45,46} For example, an aqueous RFB with a ZnCl_2 anolyte and $[\text{Fe}(\text{bpy})_3]\text{Cl}_2$ catholyte stably operates with an OCV of 1.82 V albeit in a low concentration condition of 0.1 M.⁴⁵ The low solubility of polypyridine coordination complexes in aqueous electrolytes can be improved by introducing a symmetry-breaking design of the molecular structure according to Carnelley's rule. Figure 6(b)

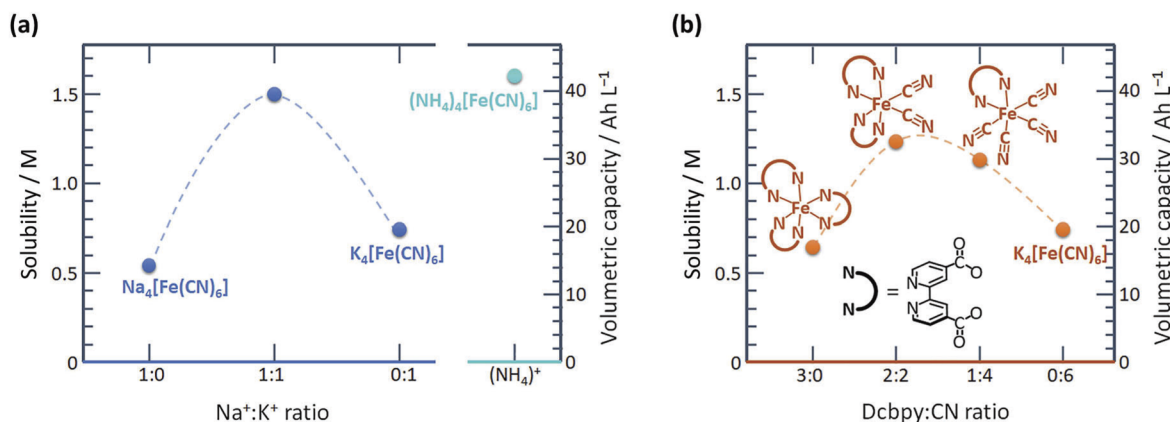


FIG. 6. Water solubility of (a) ferrocyanide salts and (b) symmetry-breaking iron complexes. Blue circles represent the data of $\text{Na}_4[\text{Fe}(\text{CN})_6]$, $\text{K}_4[\text{Fe}(\text{CN})_6]$, and the 1:1 mixture, while the cyan circle represents the $(\text{NH}_4)^+$ salt. Orange circles represent the data of $\text{K}_4[\text{Fe}(\text{Dcbpy})_x(\text{CN})_{6-2x}]$ ($x = 0-3$; Dcbpy = 2,2'-bipyridine-4,4'-dicarboxylate).

TABLE II. Iron complexes for predicting redox potentials.

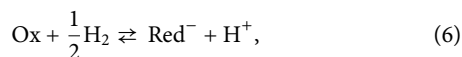
Abbreviation	Ligand	Complex (pH)	Potential/V ^a	References
bpy	2,2'-Bipyridine	[Fe ^{II} (bpy) ₃] ²⁺	1.06	22
phen	1,10-Phenanthroline	[Fe ^{II} (phen) ₃] ²⁺	1.06	22
clp	5-Chloro-1,10-phenanthroline	[Fe ^{II} (clp) ₃] ²⁺	1.21	22
mp	4-Methyl-1,10-phenanthroline	[Fe ^{II} (mp) ₃] ²⁺	0.97	22
4,7-dmp	4,7-Dimethyl-1,10-phenanthroline	[Fe ^{II} (4,7-dmp) ₃] ²⁺	0.93	22
np	5-Nitro-1,10-phenanthroline	[Fe ^{II} (np) ₃] ²⁺	1.31	22
tpy	2,2':6',6''-Terpyridine	[Fe ^{II} (tpy) ₂] ²⁺	1.06	22
tpt	2,4,6-Tris(2-pyridyl)-1,3,5-triazine	[Fe ^{II} (tpt) ₂] ²⁺	1.48	22
BIS-TRIS	2,2-Bis(hydroxymethyl)-2,2',2''-nitrilotriethanol	[Fe ^{III} (BIS-TRIS)(OH)] ⁻ (13)	-0.92	11
TEOA	Triethanolamine	[Fe ^{III} (TEOA)(OH)] ⁻ (13)	-0.86	6
DIPSO	3-[Bis(2-hydroxyethyl)amino]-2-hydroxypropanesulfonic acid	[Fe ^{III} (DIPSO)(OH)] ²⁻ (13)	-0.86	11
racEDDHA	N,N'-Ethylene-bis(o-hydroxyphenylglycine)	[Fe ^{III} (racEDDHA)] ⁻ (3-7)	-0.423	12
cit	Citrate	[Fe ^{III} (cit) ₃] (3.45)	-0.045	13
DTPA	Diethylenetriaminopentaacetate	[Fe ^{III} (DTPA)] ²⁻ (9)	0.04	14
EDTA	Ethylenediaminetetraacetate	[Fe ^{III} (EDTA)] ⁻ (5)	0.12	15
PDTA	1,3-Diaminopropanetetraacetate	[Fe ^{III} (PDTA)] ⁻ (5)	0.264	15
HEDTA	N-Hydroxyethylethylenediaminetetraacetate	[Fe ^{III} (HEDTA)] ⁻ (6)	0.349	16
mal	Malonate	[Fe ^{III} (mal) ₃] ⁺ (0.73)	0.652	17
H ₃ Tim	N,N',N''-Tris(midazole-2-ylmethyl)-1,4,7-triazacyclononane	[Fe ^{II} (H ₃ Tim) ₃] ³⁺ (3.3), [Fe ^{II} (Tim) ₃] (12.8)	0.317, -0.27	18
FcNCl	(Ferrocenylmethyl)trimethylammonium	FcN ⁺	0.61	20
C ₂ -FcNCl	(Ferrocenylethyl)trimethylammonium	C ₂ -FcN ⁺	0.44	19
C ₃ -FcNCl	(Ferrocenylpropyl)trimethylammonium	C ₃ -FcN ⁺	0.37	19
R ₂ -bpy	4,4'-Bis(R-substituted)-2,2'-bipyridine	[Fe ^{II} (R-bpy) ₃] ²⁺	-0.04	24
(R = O ⁻)			0.66	24
(R = OCH ₃)			0.86	24
(R = CH ₃)			0.985	24
(R = CH ₂ OH)			1.12	24
(R = COO ⁻)				24
		[Fe ^{II} (Bhmbpy) ₃] ²⁺		
		[Fe ^{II} (Dcbpy) ₃] ⁴⁻		

^aThe redox potential (vs SHE) calculated using the reported values.⁶

shows a comparison of the solubilities of asymmetric iron complexes and their parent compounds, $[\text{Fe}(\text{Dcbpy})_x(\text{CN})_{6-2x}]^{4-}$ ($x = 0-3$). Asymmetric $\text{K}_4[\text{Fe}(\text{Dcbpy})_2(\text{CN})_2]$ and $\text{K}_4[\text{Fe}(\text{Dcbpy})(\text{CN})_4]$ complexes have high solubilities of 1.22 M and 1.12 M, respectively, which are approximately twice as high as that of symmetric $\text{K}_4[\text{Fe}(\text{Dcbpy})_3]$ (0.6 M).²³ The solubility is an intrinsic feature of solute itself, which is independent on solvent, and correlates with the melting point.³⁴ Symmetrical molecules generally have a larger residual entropy, $R \ln \sigma$ (σ : rotational symmetry number), reducing the melting entropy.^{34,47,48}

IV. REDOX POTENTIAL

As shown in Fig. 3(a), redox potentials of iron-based complexes widely range approximately from -1 to 1.5 V (vs SHE). However, redox-active materials in aqueous catholytes/anolytes should be operated in the potential range where HER and OER are hindered.²⁰ A thermodynamic cycle or the energies of the highest occupied molecular orbital (HOMO)/lowest unoccupied molecular orbital (LUMO) from DFT calculations allow for predicting the redox potential of anolytes and catholytes.^{35,37,49} For the thermodynamic cycle, the reduction potential vs SHE is estimated by the following cell reaction:



where Ox and Red denote the oxidized and reduced states of a redox-active material, respectively. The corresponding reaction Gibbs energy $\Delta_r G$ is expressed as

$$\Delta_r G = -\mu_{\text{Ox}} - \frac{1}{2}\mu_{\text{H}_2} + \mu_{\text{Red}} + \mu_{\text{H}^+}. \quad (7)$$

For the reduction of Fe^{3+} to Fe^{2+} in the solution, the reaction Gibbs energy, $\Delta_r G_{(\text{sol})}(\text{Fe}^{3+/2+})$, includes the change in solvation energy from Fe^{3+} to Fe^{2+} ($-\Delta_{\text{solv}} G_{\text{Fe}^{3+}} + \Delta_{\text{solv}} G_{\text{Fe}^{2+}}$) in addition to

the reaction Gibbs energy from Fe^{3+} to Fe^{2+} in the gas phase [$\Delta_r G_{(\text{g})}(\text{Fe}^{3+/2+})$] as shown in Fig. 7. When $(-\mu_{\text{Ox}} + \mu_{\text{Red}})$ in Eq. (7) is defined as $\Delta_r G_{(\text{sol})}(\text{Fe}^{3+/2+})$, the redox potential E is expressed as

$$E(\text{ vs SHE}) = -\frac{\Delta_r G}{F} = -\frac{\Delta_r G_{(\text{sol})}(\text{Fe}^{3+/2+}) - \frac{1}{2}\mu_{\text{H}_2} + \mu_{\text{H}^+}}{F}. \quad (8)$$

The value of $\frac{1}{F}(-\frac{1}{2}\mu_{\text{H}_2} + \mu_{\text{H}^+})$ is often adopted as 4.44 V as recommended by IUPAC.⁵⁰ The DFT calculations provide $\Delta_r G_{(\text{sol})}(\text{Fe}^{3+/2+})$ as the total thermal energy containing the electronic energy, zero-point energy, and thermal correction. The solvation energy, for example, $\Delta_{\text{solv}} G_{\text{Fe}^{3+}}$, is calculated as the energy difference between Fe^{3+} in vacuum and solution.

Calculations at the (U)B3LYP/6-31+G* level enable accurate estimation of the standard redox potentials of metal-acetylacetonates,³⁷ bipyridine-coordinated iron complexes,⁴⁹ other iron complexes,⁵¹ and pyridinium-based organic compounds in acetonitrile.⁵² Note that the polarization continuum model (PCM) was used to estimate the solvation energy. Although multiple calculations (oxidized and reduced, in vacuum and in solvent) are necessary to obtain a redox potential, directly predicting the redox potential using the thermodynamic cycle method is highly beneficial. For example, we calculated the redox potentials of several iron complexes with polypyridine ligands in water (Table II; see Sec. VII), while the experimental redox potentials of the target compounds have already been reported for a 0.5 M sulfuric acid aqueous solution.²² As shown in Fig. 8(a), the calculated redox potentials reproduced the trend of the experimental data ($R^2 = 0.89$), indicating that the thermodynamic cycle method is a feasible approach to predict the redox potential of iron-based redox-active materials in aqueous solution. However, previous work reported a relatively large deviation from the experimental data in low-potential regions.^{37,51} Here, further improvement of the calculation method is needed, for example, by considering the actual cavity volume size of the

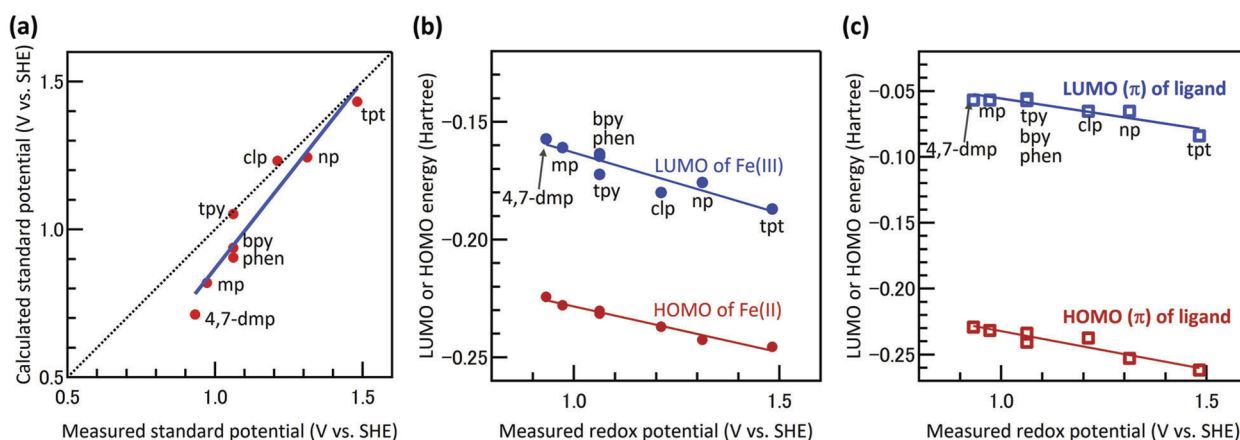


FIG. 8. (a) Correlation between the experimental and calculated standard potentials estimated by the thermodynamic cycle for polypyridine-type coordination complexes in water. The experimental values were quoted from Ref. 22. The dotted line stands for ideal linear correlation. (b) The correlation between the measured redox potentials (vs SHE) and the HOMO/LUMO energies for the iron complexes in water (red and blue circles, respectively). (c) The correlation between the measured redox potentials (vs SHE) and the π -type HOMO and LUMO energies of ligands in water (red and blue squares, respectively). The abbreviations are listed in Table II.

solute molecule because the molecular cavity size is not universal for different solutes.

HOMO and LUMO energies of the reduced and oxidized species are alternative indicators to predict a redox potential by DFT calculations. Lee *et al.* tested bipyridine-coordinated iron complexes in acetonitrile using linear regression to predict redox potentials using the LUMO energy as a discriminating feature to predict the potential ($R^2 = 0.977$).⁴⁹ Similarly, we estimated redox potentials using HOMO/LUMO features of polypyridine-coordinated iron complexes in water. The calculation result is shown in Fig. 8(b). The experimental redox potentials correspond well to the HOMO energy ($R^2 = 0.97$) of the Fe^{2+} species rather than the LUMO energy ($R^2 = 0.86$) of the Fe^{3+} species. More importantly, for the polypyridine-coordinated complexes, the redox potential correlates closely with the π -type HOMO and LUMO energies of the corresponding ligand in water ($R^2 = 0.90$ and 0.85 , respectively). Figure 9(a) shows the simplified frontier molecular orbitals of a tpy-coordinated iron complex with D_{2d} symmetry. The $d\pi$ orbitals (e and b_2) of the iron ion are coupled with the π -character orbitals (π and π^*) of the ligands.^{53–56} The DFT-calculated HOMO of $[\text{Fe}(\text{tpy})_2]^{2+}$ is delocalized onto the ligand [Fig. 9(b)], while the HOMO character corresponds to the d_{xy} orbital. A similar tendency is found in $[\text{Fe}(\text{bpy})_3]^{2+}$, where the HOMO consists of an iron d orbital and ligand π -type orbitals. Electron withdrawing groups stabilize the HOMO and LUMO energies of the substituted ligands, leading to a higher redox potential derived from the formation of a more stable iron center compared to non-substituted $[\text{Fe}(\text{bpy})_3]^{2+}$ and $[\text{Fe}(\text{tpy})_2]^{2+}$ complexes [Fig. 9(a)].

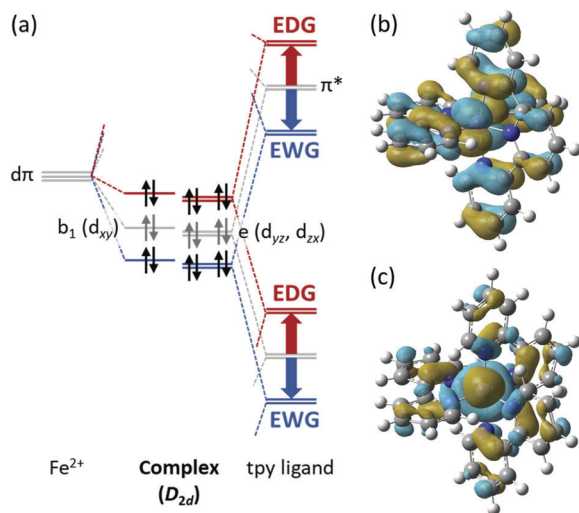


FIG. 9. (a) Frontier molecular orbital diagrams of singlet bis(tridentate) Fe^{2+} complexes {e.g., $[\text{Fe}(\text{tpy})_2]^{2+}$ } with D_{2d} symmetry. An electron-withdrawing group (EWG) on a ligand stabilizes the HOMO and LUMO energies and, hence, the electronic energy of the iron complex, leading to a higher redox potential for $\text{Fe}^{2+}/\text{Fe}^{3+}$. Electron-donating groups (EDG) lead to a lower $\text{Fe}^{2+}/\text{Fe}^{3+}$ redox potential. All σ -type orbitals are omitted for clarity. (a) HOMO of $[\text{Fe}(\text{tpy})_2]^{2+}$ complex obtained from DFT calculations in water [B3LYP/6–311+G(d,p) for Fe and 6–31G(d,p) for C, H, and N; isovalue: 0.015 a.u.]. (c) HOMO of $[\text{Fe}(\text{bpy})_3]^{2+}$ complex obtained from DFT calculations in water [B3LYP/6–311+G(d,p) for Fe and 6–31G(d,p) for C, H, and N; isovalue: 0.015 a.u.].

Conversely, ligands substituted with electron-donating groups destabilize the electronic energy of the coordination complex. High ligand HOMO and LUMO energy levels correspond to a low $\text{Fe}^{2+}/\text{Fe}^{3+}$ redox potential of the complex. Thus, DFT calculations of the ligand are useful for evaluating the redox potential of iron-based complexes.

V. STABILITY

The cycle stability of catholytes/anolytes is vital to achieve low-cost RFBs, and a capacity fade rate larger than $0.1\% \text{ day}^{-1}$ is insufficient for practical application. In general, a capacity fade results from various mechanisms, such as crossover through a membrane, electrode passivation, irreversible catholyte/anolyte decomposition, self-discharge, and capacity-imbalance between an anolyte and a catholyte⁵⁷ [Figs. 10(a)–10(f)].

Ferrocene is intrinsically stable due to an 18-electron rule. However, ferrocenium ion (oxidized ferrocene) has 17 valence electrons, leading to rapid decomposition in the presence of water and oxygen.^{58,59} For example, highly water-soluble ferrocene, FcNCl , exhibits the capacity fade rate of $0.3\% \text{ day}^{-1}$,²⁰ which is not satisfactory for practical application. However, its derivatives with 2-(trimethylammonio)ethyl and 3-(trimethylammonio)propyl groups ($\text{C}_2\text{-FcN}$ and $\text{C}_3\text{-FcN}$, respectively) improve the capacity fade rate to $0.07\% \text{ day}^{-1}$ [Fig. 10(a)].¹⁹ The decomposition mechanism of the oxidated FcN species involves the dissociation of the cyclopentadienyl, as shown in Fig. 10(c). The ligand strength in the order of $\text{C}_3\text{-FcN} > \text{C}_2\text{-FcN} > \text{FcN}$ suppresses this dissociation process of $\text{C}_3\text{-FcN}$, leading to the best cycling stability of $\text{C}_3\text{-FcN}$. Another possible explanation is that nucleophilic addition of water to the Fe^{3+} ion is suppressed due to the lower electron density on the Fe^{3+} ion of (trimethylammonio)alkyl-substituted ferrocene derivatives [Fig. 10(d)].⁶⁰

In aqueous solution, tris(bipyridine)iron complexes undergo dimerization and ligand dissociations, leading to a voltage drop and a faster capacity decay.⁶¹ However, $[\text{Fe}(\text{Bhmbpy})_3]^{2+}$ exhibits a lower capacity fade rate than $[\text{Fe}(\text{bpy})_3]^{2+}$ [Figs. 10(b) and 10(e)].²⁴ The capacity fade of $[\text{Fe}(\text{Bhmbpy})_3]^{2+}$ arises from self-discharge accompanied with the oxidation of dissociated HBhmbpy ligands. Although $[\text{Fe}(\text{Bhmbpy})_3]^{2+}$ also undergoes dimerization similar to $[\text{Fe}(\text{bpy})_3]^{2+}$, the ferric dimer can be easily recovered to the mononuclear $[\text{Fe}(\text{Bhmbpy})_3]^{2+}$ by the free HBhmbpy ligand, which is responsible for the low capacity fade rate of $0.07\% \text{ day}^{-1}$. Most likely, electro-donating groups on the bpy ligand form robust coordination bond to the Fe ion and mitigate the ligand dissociation.²²

The decomposition of ferrocyanide is well known to generate hydrocyanic gas under acidic conditions [Fig. 10(f)];⁶² thus, ferrocyanide is often applied under basic conditions. Indeed, the cycle stability tests of the ferrocyanide/ferricyanide couple in different pH conditions showed that alkaline conditions are more favorable than acidic conditions to suppress CN^- dissociation.^{63,64} A capacity decay under a strong alkaline condition (pH 14) is mainly attributable to the capacity imbalance of electrolytes due to spontaneous ferricyanide reduction at an electrode (graphite felt)–electrolyte interface [Fig. 10(f)].⁶⁴ Therefore, the ferrocyanide catholyte best operates under a neutral pH and dark to avoid undesirable side reactions.

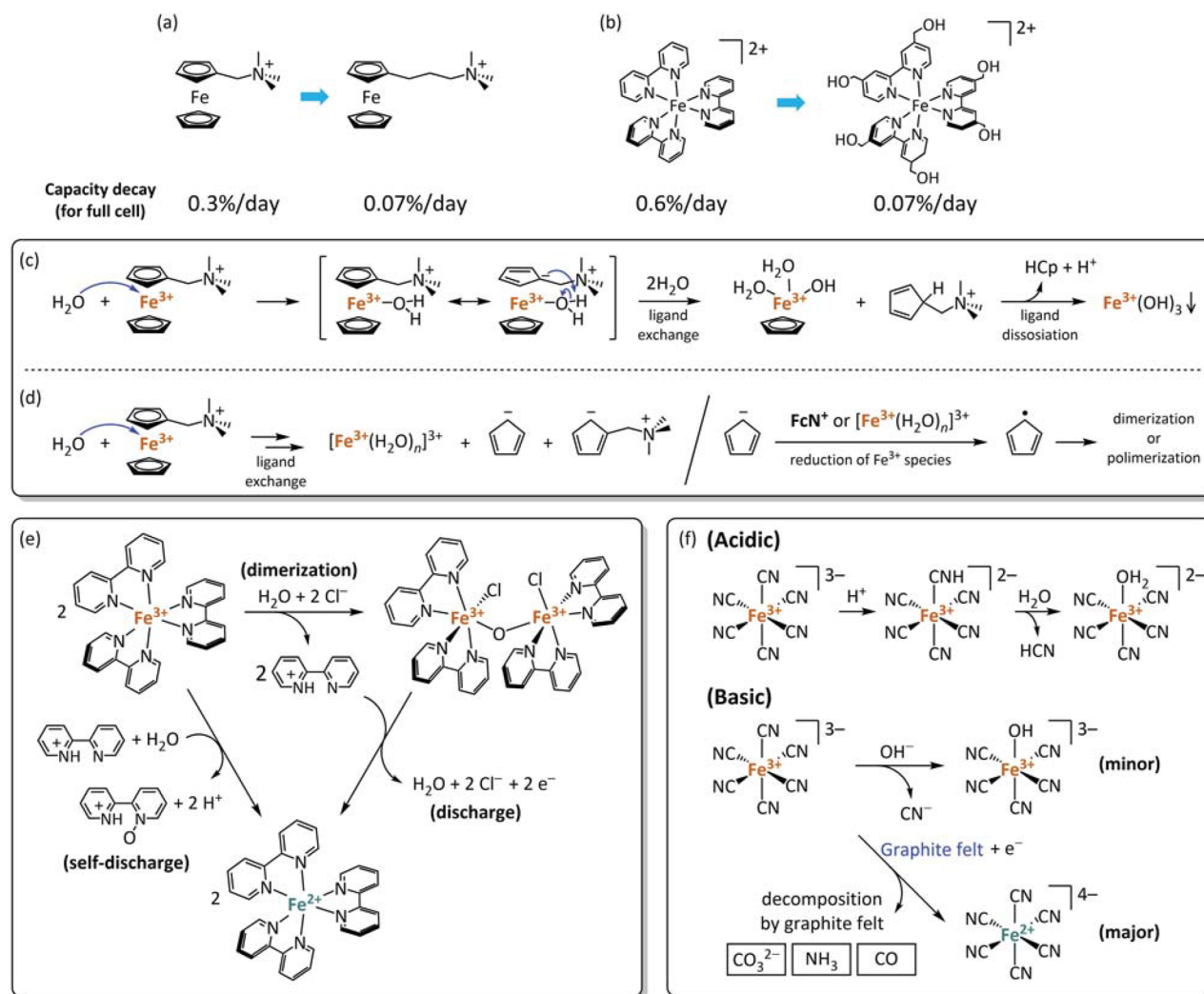


FIG. 10. Schematic representation of improvement of capacity decay for RFBs using (a) ferrocene alkylammonium derivatives and (b) tris(bipyridine)iron ones as catholyte. (c)–(f) Proposed degradation mechanisms of (c) and (d) FcN^+ , (e) tris(bipyridine)iron, and (f) ferrocyanide/ferricyanide.

VI. SUMMARY AND OUTLOOK

We described iron-based catholytes for aqueous RFBs from the viewpoint of solubility, redox potential, and stability. From the energy density perspective, catholytes with a high redox potential and high solubility are desirable for the wide deployment of aqueous RFBs in a power grid. Polypyridine-coordinated iron complexes possess a reasonable redox potential of ~ 1 V (vs SHE), conforming to the cathodic potential limit of the electrochemical window of aqueous systems with carbonaceous current collectors. Thus, derivatives of $[\text{Fe}(\text{bpy})_3]^{2+}$ and $[\text{Fe}(\text{tpy})_2]^{2+}$ are promising candidates for high-performance catholytes. Introducing substituents on the ligands of iron-based catholytes is an effective way to modulate the redox potential. Substitution can also contribute to improving solubility, for example, by exploiting hydrophilic groups and a

symmetry-breaking molecular design (Fig. 11). Compared to the relevant homoleptic compounds, heteroleptic complexes adopt asymmetric structures, facilitating the preparation of a higher condensed solution. Some previous reports focused on heteroleptic tpy-coordinated iron complexes using anhydrous iron halides.^{65–69}

To enhance cyclability, spectroscopic studies are important to clarify the chemical degradation mechanism of redox-active materials and electrolytes. In particular, *in situ* characterization will open the door to further optimization of electrolytes for high-performance RFBs. For example, Gray and co-workers recently demonstrated a state-of-the-art *in situ* characterization technique using nuclear magnetic resonance techniques to reveal the decomposition mechanism of anthraquinone anolytes in aqueous RFBs.⁷⁰ Other measurements, such as electron spin resonance,^{71–73} optical,^{74–78} infrared,^{79–82} and Raman,^{83–85} spectroscopies, are also

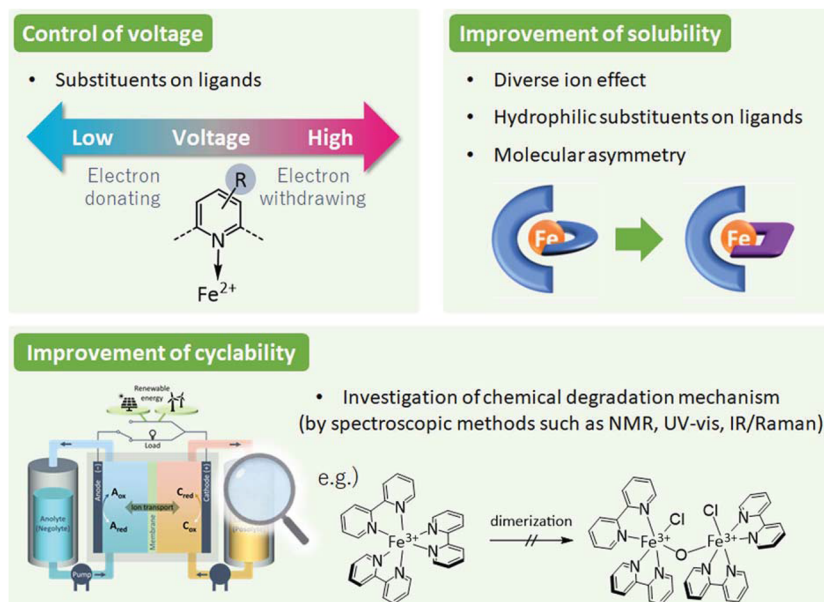


FIG. 11. Molecular design strategy of iron-based catholytes for advanced aqueous RFBs with improved voltage, solubility, and cyclability.

suitable for investigating capacity decay mechanisms. The comprehensive understandings of both physicochemical and electrochemical properties would provide a rationale to develop advanced aqueous RFBs using better iron-based catholytes.

VII. METHODS

To estimate the standard potentials of polypyridine-coordinated iron complexes, DFT calculations were performed using the Gaussian 16W package.⁸⁶ The doublet ($S = 1/2$) Fe^{3+} species were calculated using a hybrid functional, B3LYP, containing the Becke exchange⁸⁷ and the Lee–Yang–Parr correlation functionals,⁸⁸ while an unrestricted hybrid functional, UB3LYP, was applied to the singlet ($S = 0$) Fe^{2+} species. The 6–311+G(d,p) and 6–31G(d,p) basis sets were used for Fe and all nonmetallic atoms, respectively. The minimized structures of the geometry optimizations in vacuum were confirmed by frequency analysis calculations. The $\Delta_r G_{(g)}(\text{Fe}^{3+/2+})$ values were evaluated as the Gibbs energy differences between the reduced and oxidized iron species with zero-point energy and thermal corrections. To estimate the solvation energies, the single-point energies of the complexes in water were calculated by applying the PCM⁸⁹ model to the gas-phase optimized geometries of the corresponding species. The solvation energies $\Delta_{\text{solv}} G_{\text{Fe}^{3+}}$ and $\Delta_{\text{solv}} G_{\text{Fe}^{2+}}$ were adopted as the energy differences between the corresponding species in vacuum and in solution, which were corrected with zero-point energy. The standard potentials were obtained from Eq. (7), where the solvation energy of the electrons is approximated as zero.

DFT calculations of the ligands were performed at the B3LYP/6–31G(d,p) level. The LUMO and HOMO energies in Fig. 8(c) are π -type orbitals. Furthermore, we plotted the energy value of the HOMO + 1 for the np ligand because the LUMO

was mainly localized on the nitro group. For the bpy and tpy ligands, optimized molecular structures were obtained as saddle points where the ligand structure had a coplanar conformation between pyridine rings.

ACKNOWLEDGMENTS

The authors thank Dr. T. Abe (The Univ. of Tokyo) for helpful discussions on DFT calculations.

AUTHOR DECLARATIONS

Conflict of Interest

The authors have no conflicts to disclose.

Author Contributions

Atsushi Okazawa: Supervision (equal); Writing – original draft (equal); Writing – review & editing (equal). **Takayuki Kakuchi:** Writing – review & editing (equal). **Kosuke Kawai:** Writing – review & editing (equal). **Masashi Okubo:** Supervision (equal); Writing – original draft (equal); Writing – review & editing (equal).

DATA AVAILABILITY

The data that support the findings of this study are available from the corresponding author upon reasonable request.

REFERENCES

- B. Dunn, H. Kamath, and J. M. Tarascon, *Science* **334**, 928–935 (2011).
- J. W. Choi and D. Aurbach, *Nat. Rev. Mater.* **1**, 16013 (2016).
- E. A. Olivetti, G. Ceder, G. G. Gaustad, and X. Fu, *Joule* **1**, 229–243 (2017).

- ⁴K. Liu, Y. Liu, D. Lin, A. Pei, and Y. Cui, *Sci. Adv.* **4**, eaas9820 (2018).
- ⁵M. Skylas-Kazacos, M. Rychcik, R. G. Robins, A. G. Fane, and M. A. Green, *J. Electrochem. Soc.* **133**, 1057–1058 (1986).
- ⁶K. Gong, F. Xu, J. B. Grunewald, X. Ma, Y. Zhao, S. Gu, and Y. Yan, *ACS Energy Lett.* **1**, 89–93 (2016).
- ⁷K. Lin, Q. Chen, M. R. Gerhardt, L. Tong, S. B. Kim, L. Eisenach, A. W. Valle, D. Hardee, R. G. Gordon, M. J. Aziz, and M. P. Marshak, *Science* **349**, 1529–1532 (2015).
- ⁸T. Liu, X. Wei, Z. Nie, V. Sprenkle, W. Wang, T. Liu, X. Wei, Z. Nie, V. Sprenkle, and W. Wang, *Adv. Energy Mater.* **6**, 1501449 (2016).
- ⁹T. Janoschka, N. Martin, U. Martin, C. Friebe, S. Morgenstern, H. Hiller, M. D. Hager, and U. S. Schubert, *Nature* **527**, 78–81 (2015).
- ¹⁰L. W. Hruska and R. F. Savinell, *J. Electrochem. Soc.* **128**, 18–25 (1981).
- ¹¹M. Shin, C. Noh, Y. Chung, and Y. Kwon, *Chem. Eng. J.* **398**, 125631 (2020).
- ¹²P. Schröder, D. Obendorf, and T. Bechtold, *ChemElectroChem* **6**, 3311–3318 (2019).
- ¹³Y. H. Wen, H. M. Zhang, P. Qian, H. T. Zhou, P. Zhao, B. L. Yi, and Y. S. Yang, *J. Electrochem. Soc.* **153**, A929 (2006).
- ¹⁴S. E. Waters, B. H. Robb, and M. P. Marshak, *ACS Energy Lett.* **5**, 1758–1762 (2020).
- ¹⁵H. Ogino, T. Nagata, and K. Ogino, *Inorg. Chem.* **28**, 3656–3659 (1989).
- ¹⁶J. G. Ibanez, C. Choi, and R. S. Becker, *J. Electrochem. Soc.* **134**, 3083–3089 (1987).
- ¹⁷K. L. Hawthorne, J. S. Wainright, and R. F. Savinell, *J. Electrochem. Soc.* **161**, A1662–A1671 (2014).
- ¹⁸P. B. Tsitovich, A. M. Kosswattaarachchi, M. R. Crawley, T. Y. Tittiris, T. R. Cook, and J. R. Morrow, *Chem. - Eur. J.* **23**, 15327–15331 (2017).
- ¹⁹J. Luo, M. Hu, W. Wu, B. Yuan, and T. L. Liu, *Energy Environ. Sci.* **15**, 1315–1324 (2022).
- ²⁰B. Hu, C. Debruler, Z. Rhodes, and T. L. Liu, *J. Am. Chem. Soc.* **139**, 1207–1214 (2017).
- ²¹E. S. Beh, D. De Porcellinis, R. L. Gracia, K. T. Xia, R. G. Gordon, and M. J. Aziz, *ACS Energy Lett.* **2**, 639–644 (2017).
- ²²Y. D. Chen, K. S. V. Santhanam, and A. J. Bard, *J. Electrochem. Soc.* **128**, 1460–1467 (1981).
- ²³X. Li, P. Gao, Y. T. Lai, J. D. Bazak, A. Hollas, H. Y. Lin, V. Murugesan, S. Zhang, C. F. Cheng, W. Y. Tung, Y. Y. T. Lai, R. Feng, J. Wang, C. L. Wang, W. Wang, and Y. Zhu, *Nat. Energy* **6**, 873–881 (2021).
- ²⁴J. Gao, K. Amini, T. Y. George, Y. Jing, T. Tsukamoto, D. Xi, R. G. Gordon, and M. J. Aziz, *Adv. Energy Mater.* **12**, 2202444 (2022).
- ²⁵P. Schröder, N. Aguiló-Aguayo, D. Obendorf, and T. Bechtold, *Electrochim. Acta* **430**, 141042 (2022).
- ²⁶M. Shin, S. Oh, H. Jeong, C. Noh, Y. Chung, J. W. Han, and Y. Kwon, *Int. J. Energy Res.* **46**, 8175–8185 (2022).
- ²⁷C. Noh, Y. Chung, and Y. Kwon, *J. Power Sources* **495**, 229799 (2021).
- ²⁸M. Park, J. Ryu, W. Wang, and J. Cho, *Nat. Rev. Mater.* **2**, 16080 (2016).
- ²⁹P. Leung, A. A. Shah, L. Sanz, C. Flox, J. R. Morante, Q. Xu, M. R. Mohamed, C. Ponce de León, and F. C. Walsh, *J. Power Sources* **360**, 243–283 (2017).
- ³⁰D. G. Kwabi, Y. Ji, and M. J. Aziz, *Chem. Rev.* **120**, 6467–6489 (2020).
- ³¹R. Schmid, *Monatsh. Chem.* **132**, 1295–1326 (2001).
- ³²R. J. C. Brown and R. F. C. Brown, *J. Chem. Educ.* **77**, 724 (2000).
- ³³R. Pinal, *Org. Biomol. Chem.* **2**, 2692–2699 (2004).
- ³⁴D. S. Palmer, A. Llinàs, I. Morao, G. M. Day, J. M. Goodman, R. C. Glen, and J. B. O. Mitchell, *Mol. Pharm.* **5**, 266–279 (2008).
- ³⁵L. Cheng, R. S. Assary, X. Qu, A. Jain, S. P. Ong, N. N. Rajput, K. Persson, and L. A. Curtiss, *J. Phys. Chem. Lett.* **6**, 283–291 (2015).
- ³⁶S. Er, C. Suh, M. P. Marshak, and A. Aspuru-Guzik, *Chem. Sci.* **6**, 885–893 (2015).
- ³⁷J. F. Kucharyson, L. Cheng, S. O. Tung, L. A. Curtiss, and L. T. Thompson, *J. Mater. Chem. A* **5**, 13700–13709 (2017).
- ³⁸J. Luo, B. Hu, C. Debruler, Y. Bi, Y. Zhao, B. Yuan, M. Hu, W. Wu, and T. L. Liu, *Joule* **3**, 149–163 (2019).
- ³⁹G. Wang, H. Zou, Z. Xu, A. Tang, F. Zhong, X. Zhu, C. Qin, M. Ding, W. You, and C. Jia, *Mater. Today Energy* **28**, 101061 (2022).
- ⁴⁰X. Xing, Y. Zhao, and Y. Li, *J. Power Sources* **293**, 778–783 (2015).
- ⁴¹J. H. Kim, K. J. Kim, M. S. Park, N. J. Lee, U. Hwang, H. Kim, and Y. J. Kim, *Electrochem. Commun.* **13**, 997–1000 (2011).
- ⁴²C. X. Cammack, H. D. Pratt, L. J. Small, and T. M. Anderson, *Dalton Trans.* **50**, 858–868 (2021).
- ⁴³J. Mun, D.-J. Oh, M. S. Park, O. Kwon, H.-T. Kim, S. Jeong, Y. G. Kim, and M.-J. Lee, *J. Electrochem. Soc.* **165**, A215–A219 (2018).
- ⁴⁴C. Chen, S. Zhang, Y. Zhu, Y. Qian, Z. Niu, J. Ye, Y. Zhao, and X. Zhang, *RSC Adv.* **8**, 18762–18770 (2018).
- ⁴⁵Z. Xie, L. Wei, and S. Zhong, *Front. Mater. Sci.* **14**, 442–449 (2020).
- ⁴⁶W. Ruan, J. Mao, S. Yang, and Q. Chen, *J. Electrochem. Soc.* **167**, 100543 (2020).
- ⁴⁷S. H. Yalkowsky, J. F. Krzyzaniak, and P. B. Myrdal, *Ind. Eng. Chem. Res.* **33**, 1872–1877 (1994).
- ⁴⁸R.-M. Dannenfelser and S. H. Yalkowsky, *Ind. Eng. Chem. Res.* **35**, 1483–1486 (1996).
- ⁴⁹H. Kim, J. Park, and Y. S. Lee, *J. Comput. Chem.* **36**, 33–41 (2015).
- ⁵⁰S. T. Trasatti, *Pure Appl. Chem.* **58**, 955–966 (1986).
- ⁵¹H. Kim, J. Park, and Y. S. Lee, *J. Comput. Chem.* **34**, 2233–2241 (2013).
- ⁵²C. S. Sevov, D. P. Hickey, M. E. Cook, S. G. Robinson, S. Barnett, S. D. Minter, M. S. Sigman, and M. S. Sanford, *J. Am. Chem. Soc.* **139**, 2924–2927 (2017).
- ⁵³T. Ayers, S. Scott, J. Goins, N. Caylor, D. Hathcock, S. J. Slattery, and D. L. Jameson, *Inorg. Chim. Acta* **307**, 7–12 (2000).
- ⁵⁴R. R. Ruminski, J. Nelson, and W. Culver, *Inorg. Chim. Acta* **357**, 839–844 (2004).
- ⁵⁵M. Papp, T. Keszthelyi, A. Vancza, É. G. Bajnóczi, É. Kovács, Z. Németh, C. Bogdán, G. Bazsó, T. Rozgonyi, and G. Vankó, *Inorg. Chem.* **62**, 6397–6410 (2023).
- ⁵⁶K. G. von Eschwege and J. Conradie, *Electrochem. Commun.* **136**, 107225 (2022).
- ⁵⁷T. Kong, J. Liu, X. Zhou, J. Xu, Y. Xie, J. Chen, X. Li, and Y. Wang, *Angew. Chem., Int. Ed.* **62**, e202214819 (2023).
- ⁵⁸A. Singh, D. R. Chowdhury, and A. Paul, *Analyst* **139**, 5747–5754 (2014).
- ⁵⁹G. Zotti, G. Schiavon, S. Zecchin, and D. Favretto, *J. Electroanal. Chem.* **456**, 217–221 (1998).
- ⁶⁰Q. Chen, Y. Li, Y. Liu, P. Sun, Z. Yang, and T. Xu, *ChemSusChem* **14**, 1295–1301 (2021).
- ⁶¹N. E. Holubowitch and G. Nguyen, *Inorg. Chem.* **61**, 9541–9556 (2022).
- ⁶²I. M. Kolthoff and E. A. Pearson, *Ind. Eng. Chem., Anal. Ed.* **3**, 381–382 (1931).
- ⁶³J. Luo, A. Sam, B. Hu, C. DeBruler, X. Wei, W. Wang, and T. L. Liu, *Nano Energy* **42**, 215–221 (2017).
- ⁶⁴M. Hu, A. P. Wang, J. Luo, Q. Wei, and T. L. Liu, *Adv. Energy Mater.* **13**, 2203762 (2023).
- ⁶⁵Y. Miyamoto, A. Kikuchi, F. Iwahori, and J. Abe, *J. Phys. Chem. A* **109**, 10183–10188 (2005).
- ⁶⁶M. Gagliardo, J. Perelaer, F. Hartl, G. P. M. van Klink, and G. van Koten, *Eur. J. Inorg. Chem.* **2007**, 2111–2120.
- ⁶⁷W. Yan, C. Réthoré, S. Menning, G. Brenner-Weiß, T. Müller, P. Pierrat, and S. Bräse, *Chem. - Eur. J.* **22**, 11522–11526 (2016).
- ⁶⁸D. J. Hathcock, K. Stone, J. Madden, and S. J. Slattery, *Inorg. Chim. Acta* **282**, 131–135 (1998).
- ⁶⁹Y. W. Zhong, N. Vila, J. C. Henderson, S. Flores-Torres, and H. D. Abruña, *Inorg. Chem.* **46**, 10470–10472 (2007).
- ⁷⁰E. W. Zhao, T. Liu, E. Jónsson, J. Lee, I. Temprano, R. B. Jethwa, A. Wang, H. Smith, J. Carretero-González, Q. Song, and C. P. Grey, *Nature* **579**, 224–228 (2020).
- ⁷¹R. Feng, X. Zhang, V. Murugesan, A. Hollas, Y. Chen, Y. Shao, E. Walter, N. P. N. Wellala, L. Yan, K. M. Rosso, and W. Wang, *Science* **372**, 836–840 (2021).
- ⁷²E. W. Zhao, E. Jónsson, R. B. Jethwa, D. Hey, D. Lyu, A. Brookfield, P. A. A. Klusener, D. Collison, and C. P. Grey, *J. Am. Chem. Soc.* **143**, 1885–1895 (2021).
- ⁷³Y. Zhang, F. Li, T. Li, M. Zhang, Z. Yuan, G. Hou, J. Fu, C. Zhang, and X. Li, *Energy Environ. Sci.* **16**, 231–240 (2023).
- ⁷⁴L. Tong, Q. Chen, A. A. Wong, R. Gómez-Bombarelli, A. Aspuru-Guzik, R. G. Gordon, and M. J. Aziz, *Phys. Chem. Chem. Phys.* **19**, 31684–31691 (2017).
- ⁷⁵N. E. Holubowitch and A. Jabbar, *Microchem. J.* **182**, 107920 (2022).

- ⁷⁶N. Aguiló-Aguayo and T. Bechtold, *J. Electrochem. Soc.* **165**(13), A3164–A3168 (2018).
- ⁷⁷R. P. Brooker, C. J. Bell, L. J. Bonville, H. R. Kunz, and J. M. Fenton, *J. Electrochem. Soc.* **162**, A608–A613 (2015).
- ⁷⁸Z. Tang, D. S. Aaron, A. B. Papandrew, and T. A. Zawodzinski, *ECS Trans.* **41**, 1–9 (2012).
- ⁷⁹O. Nolte, R. Geitner, M. D. Hager, and U. S. Schubert, *Adv. Energy Mater.* **11**, 2100931 (2021).
- ⁸⁰E. V. Carino, J. Staszak-Jirkovsky, R. S. Assary, L. A. Curtiss, N. M. Markovic, and F. R. Brushett, *Chem. Mater.* **28**, 2529–2539 (2016).
- ⁸¹Z. Li and Y.-C. Lu, *Nat. Energy* **6**, 517–528 (2021).
- ⁸²C. O. Wilhelmsen, S. B. Kristensen, O. Nolte, I. A. Volodin, J. V. Christiansen, T. Isbrandt, T. Sørensen, C. Petersen, T. E. Sondergaard, K. Lehmann Nielsen, T. O. Larsen, J. C. Frisvad, M. D. Hager, U. S. Schubert, J. Muff, and J. L. Sørensen, *Batteries Supercaps* **6**, e202200365 (2023).
- ⁸³H. J. Lee, D.-W. Kim, and J. H. Yang, *J. Electrochem. Soc.* **164**, A754–A759 (2017).
- ⁸⁴A. S. Danis, M. J. Counihan, K. O. Hatfield, J. Zhang, G. Agarwal, L. Zhang, R. S. Assary, and J. Rodríguez-López, *Electrochim. Acta* **447**, 142123 (2023).
- ⁸⁵Y. Liu, G. H. Wen, J. Liang, S. S. Bao, J. Wei, H. Wang, P. Zhang, M. Zhu, Q. Jia, J. Ma, L. M. Zheng, and Z. Jin, *ACS Energy Lett.* **8**, 387–397 (2022).
- ⁸⁶M. J. Frisch, G. W. Trucks, H. B. Schlegel, G. E. Scuseria, M. A. Robb, J. R. Cheeseman, G. Scalmani, V. Barone, G. A. Petersson, H. Nakatsuji, X. Li, M. Caricato, A. V. Marenich, J. Bloino, B. G. Janesko, R. Gomperts, B. Mennucci, H. P. Hratchian, J. V. Ortiz, A. F. Izmaylov, J. L. Sonnenberg, D. Williams-Young, F. Ding, F. Lipparini, F. Egidi, J. Goings, B. Peng, A. Petrone, T. Henderson, D. Ranasinghe, V. G. Zakrzewski, J. Gao, N. Rega, G. Zheng, W. Liang, M. Hada, M. Ehara, K. Toyota, R. Fukuda, J. Hasegawa, M. Ishida, T. Nakajima, Y. Honda, O. Kitao, H. Nakai, T. Vreven, K. Throssell, J. A. Montgomery, Jr., J. E. Peralta, F. Ogliaro, M. J. Bearpark, J. J. Heyd, E. N. Brothers, K. N. Kudin, V. N. Staroverov, T. A. Keith, R. Kobayashi, J. Normand, K. Raghavachari, A. P. Rendell, J. C. Burant, S. S. Iyengar, J. Tomasi, M. Cossi, J. M. Millam, M. Klene, C. Adamo, R. Cammi, J. W. Ochterski, R. L. K. Martin, O. Morokuma, J. B. Farkas Foresman, and D. J. Fox, *Gaussian 16, Revision C.01*, Gaussian, Inc., Wallingford, CT, 2016.
- ⁸⁷A. D. Becke, *J. Chem. Phys.* **98**, 5648–5652 (1993).
- ⁸⁸C. Lee, W. Yang, and R. G. Parr, *Phys. Rev. B* **37**, 785–789 (1988).
- ⁸⁹S. Miertuš, E. Scrocco, and J. Tomasi, *Chem. Phys.* **55**, 117–129 (1981).